

Further analysis of multilevel Stein variational gradient descent with an application to the Bayesian inference of glacier ice models

Terrence Alsup* Tucker Hartland† Benjamin Peherstorfer*
 Noemi Petra†

December 8, 2022

Multilevel Stein variational gradient descent is a method for particle-based variational inference that leverages hierarchies of approximations of target distributions with varying costs and fidelity to computationally speed up inference. This work provides a cost complexity analysis of multilevel Stein variational gradient descent that applies under milder conditions than previous results, especially in discrete-in-time regimes and beyond the limited settings where Stein variational gradient descent achieves exponentially fast convergence. The analysis shows that the convergence rate of Stein variational gradient descent enters only as a constant factor for the cost complexity of the multilevel version, which means that the costs of the multilevel version scale independently of the convergence rate of Stein variational gradient descent on a single level. Numerical experiments with Bayesian inverse problems of inferring discretized basal sliding coefficient fields of the Arolla glacier ice demonstrate that multilevel Stein variational gradient descent achieves orders of magnitude speedups compared to its single-level version.

Keywords: Multi-fidelity and multilevel methods, Bayesian inference, Stein variational gradient descent, ice sheet inverse problems

1 Introduction

Bayesian inference is a ubiquitous and flexible tool for updating a belief (i.e., learning) about a quantity of interest when data are observed, which ultimately can be used to inform upstream decision-making. In particular, Bayesian inverse problems allow one to derive knowledge from data through the lens of physics-based models. These problems can be formulated as follows: given observational data, a physics-based model, and prior information about the model inputs, find a posterior probability distribution for the inputs that reflects the knowledge about the inputs in terms of the observed data and prior. Typically, the physics-based models are given in the form of an input-to-observation map that is based on a system of partial differential equations (PDEs). The computational task underlying Bayesian inference is approximating the posterior probability distributions to compute expectations and to quantify uncertainties. There are multiple ways of computationally exploring the posterior distribution to gain insights, reaching from Markov chain Monte Carlo to variational methods [24, 42, 28].

*Courant Institute of Mathematical Sciences, New York University, NY, USA

†Department of Applied Mathematics, University of California, Merced, CA, USA

In this work, we make use of Stein variational gradient descent (SVGD) [32], which is a method for particle-based variational inference, to approximate posterior distributions. It builds on Stein’s identity to formulate an update step for the particles that can be realized numerically in an efficient manner via a reproducing kernel Hilbert space. There are various extensions to SVGD such as exploiting curvature information of the target distribution with a corresponding Newton method [14] as well as using adaptive kernels as in [16, 47]. Specifically for Bayesian inverse problems, SVGD has been extended to take advantage of low-dimensional structure [13] in the posterior distribution [9] and the model states [8]. Much effort has been put into understanding the convergence and statistical properties of SVGD and its variants. The study of convergence of SVGD was sparked primarily by [31, 33], which showed that in the mean-field limit SVGD follows a gradient flow with respect to the Kullback-Leibler (KL) divergence. Similar results were later shown for the chi-squared divergence in [10]. Pre-asymptotic convergence results in both the number of samples and the discrete-time setting remains open, but progress in this direction has been made in [27]. There also has been work on understanding and improving the performance of SVGD in high dimensions [4].

We focus on the multilevel extension of SVGD (MLSVGD), which was introduced in [3] and leverages hierarchies of approximations of the target posterior distributions with varying costs and fidelity to computationally speed up inference. Such approximations can be obtained via, e.g., coarse and fine discretizations of the governing equations of the physics-based models as well as surrogate models [40] and simplified-physics models [26]. Multilevel methods have a long tradition in scientific computing and computational statistics. The MLSVGD approach is motivated by multi-fidelity and multilevel methods such as multilevel and multi-fidelity Monte Carlo [21, 17, 11, 37, 36] and Markov chain Monte Carlo (MCMC) methods [15, 34, 39]. The MLSVGD also shares similarities with multilevel sequential Monte Carlo [5, 29, 46, 38] and importance sampling [2, 40, 46], multilevel particle filters [18], multilevel preconditioning [6, 20, 30], and multilevel ensemble Kalman methods [22, 7], which all use hierarchies of surrogate models to generate samples sequentially. The work [3] provides a cost complexity analysis of MLSVGD that shows speedups compared to single-level SVGD; but it relies on the continuous-time limit and an exponential convergence rate of SVGD and thus is limited in scope.

In this work, we contribute an analysis of MLSVGD that applies to a discrete-in-time formulation, rather than only to the continuous-in-time limit as the analysis provided in [3]. The finding is that the same cost complexity is achieved as in the continuous-time setting as long as the stepsize decays sufficiently fast. We also provide the cost complexity for a general rate of convergence of SVGD with respect to the KL divergence rather than just an exponential rate, which increases the scope of the cost complexity analysis to a wider range of settings where SVGD is used. We show that MLSVGD achieves speedup over traditional SVGD when the convergence rate of SVGD is slow. This is directly applicable to Bayesian inverse problems, where we show that the assumptions of the cost complexity analysis are satisfied in typical settings.

We numerically demonstrate MLSVGD on a Bayesian inverse problem of inferring a discretized basal sliding coefficient field from velocity observations at the surface of the Arolla glacier [41]; see also [35]. The numerical setup builds on FEniCS [1] and hippylib [43, 44, 45, 25], which allows for fast gradient-based inference via adjoints. The numerical results show that MLSVGD performs inference at a fraction of the cost of inference with SVGD and that it leads to higher quality particles with respect to the maximum mean discrepancy (MMD) [19] than samples obtained with a variant of MCMC.

The manuscript is organized as follows. In Section 2 we outline preliminaries on Bayesian inverse problems, SVGD, and previous work on MLSVGD. Section 3 introduces new cost complexity bounds for MLSVGD that apply in more general settings, in particular the discrete-time setting. In Section 4 we demonstrate improvements by several factors in terms of computational savings for MLSVGD over SVGD for inferring the basal sliding coefficient in the Arolla glacier ice model. We conclude in Section 5.

2 Preliminaries

In this section, Bayesian inverse problems are reviewed and it is discussed how they are related to sampling from a target distribution with, e.g., SVGD and MLSVGD.

2.1 Bayesian inverse problems

Let $G : \Theta \rightarrow \mathbb{R}^q$ denote a parameter-to-observable map and consider noisy data $\mathbf{y} = G(\boldsymbol{\theta}^*) + \boldsymbol{\eta}$, where $\boldsymbol{\eta} \sim N(\mathbf{0}, \Gamma)$ with known noise covariance matrix $\Gamma \in \mathbb{R}^{q \times q}$ and $\boldsymbol{\theta}^* \in \Theta \subset \mathbb{R}^d$. Given a prior $\pi_0 : \Theta \rightarrow \mathbb{R}$, the target posterior density is

$$\pi(\boldsymbol{\theta}) \propto \exp\left(-\frac{1}{2} \|\mathbf{y} - G(\boldsymbol{\theta})\|_{\Gamma^{-1}}^2\right) \pi_0(\boldsymbol{\theta}),$$

where $\|\mathbf{v}\|_{\Gamma^{-1}}^2 = \langle \mathbf{v}, \Gamma^{-1} \mathbf{v} \rangle$. In many computational science and engineering applications, the parameter-to-observable map G depends on the solution of an underlying system of PDEs, which means that it cannot be evaluated directly. Instead, one must resort to a numerical method that discretizes the underlying PDE problem to approximately evaluate G . Let $G^{(\ell)}$ be such an approximate parameter-to-observable map, where the index ℓ denotes the fidelity and corresponds to, e.g., the mesh width or number of grid points. The larger ℓ , the more accurate the approximation $G^{(\ell)}$ of G in the following. The corresponding low-fidelity posterior is

$$\pi^{(\ell)}(\boldsymbol{\theta}) \propto \exp\left(-\frac{1}{2} \|\mathbf{y} - G^{(\ell)}(\boldsymbol{\theta})\|_{\Gamma^{-1}}^2\right) \pi_0(\boldsymbol{\theta}). \quad (1)$$

Increasing the level ℓ , gives rise to a sequence of densities $(\pi^{(\ell)})_{\ell=1}^{\infty}$ that converges pointwise $\pi^{(\ell)}(\boldsymbol{\theta}) \rightarrow \pi(\boldsymbol{\theta})$ for every $\boldsymbol{\theta} \in \Theta$ so that the sequence of random variables $\boldsymbol{\theta}^{(\ell)} \sim \pi^{(\ell)}$ converges weakly to $\boldsymbol{\theta} \sim \pi$.

Our aim is to compute quantities of interest of the form

$$\mathbb{E}_{\pi}[f] = \int_{\Theta} f(\boldsymbol{\theta}) d\pi(\boldsymbol{\theta}), \quad (2)$$

for given test functions $f : \Theta \rightarrow \mathbb{R}$. Because π is not readily available, one typically selects a sufficiently accurate $G^{(L)}$ and approximates the quantity of interest with respect to the corresponding density $\pi^{(L)}$,

$$\mathbb{E}_{\pi^{(L)}}[f] = \int_{\Theta} f(\boldsymbol{\theta}) d\pi^{(L)}(\boldsymbol{\theta}). \quad (3)$$

A well-established approach to estimate (3) using Monte Carlo involves drawing samples $\boldsymbol{\theta}^{[1]}, \dots, \boldsymbol{\theta}^{[N]}$ of the distribution with density $\pi^{(L)}$ and computing

$$\hat{f} = \frac{1}{N} \sum_{i=1}^N f(\boldsymbol{\theta}^{[i]}). \quad (4)$$

For example, the samples $\boldsymbol{\theta}^{[1]}, \dots, \boldsymbol{\theta}^{[N]}$ may be i.i.d. or come from a realization of an ergodic Markov chain. This gives rise to two sources of error with respect to the quantity of interest (2). The first source of error is the Monte Carlo error of estimating the expectation in (3) with (4), while the second source of error is due to using the deterministic approximation $G^{(L)}$ of G , and thus $\pi^{(L)}$ instead of π . The Monte Carlo error can be controlled with the number of samples N . The second error is controlled by the level L , which can be selected via, e.g., the Hellinger distance so that

$$d_{\text{Hell}}\left(\pi^{(L)}, \pi\right) \leq \epsilon$$

holds for some tolerance $\epsilon > 0$. The Hellinger distance is particularly useful because it is a metric on the space of probability measures, allowing to separate the deterministic error due to the fidelity and the statistical error due to sampling, and can be bounded from above by the KL divergence

$$2d_{\text{Hell}}(\mu_1, \mu_2)^2 \leq \text{KL}(\mu_1 \parallel \mu_2). \quad (5)$$

2.2 Stein variational gradient descent

We now briefly review SVGD [32] that aims to derive a sequence of distributions to minimize the KL divergence with respect to the target density $\pi^{(L)}$. Once convergence has been reached, the quantity of interest (2) can be estimated using particles of the distribution.

Let \mathcal{H} be a reproducing kernel Hilbert space (RKHS) with positive definite kernel $K : \Theta \times \Theta \rightarrow \mathbb{R}$ of functions $g : \Theta \rightarrow \mathbb{R}$ and let $\mathcal{H}^d \simeq \mathcal{H} \times \dots \times \mathcal{H}$ be the corresponding RKHS of vector fields $\mathbf{g} = (g_1, \dots, g_d) : \Theta^d \rightarrow \mathbb{R}^d$. Define the KL functional

$$J_\mu(\mathbf{g}) = \text{KL} \left((\mathbf{I} - \mathbf{g})_\# \mu \parallel \pi^{(L)} \right),$$

where $(\mathbf{I} - \mathbf{g})_\# \mu$ denotes the pushforward measure of μ under the map $\mathbf{I} - \mathbf{g}$, so that if $\boldsymbol{\theta} \sim \mu$, then $\boldsymbol{\theta} - \mathbf{g}(\boldsymbol{\theta}) \sim (\mathbf{I} - \mathbf{g})_\# \mu$, with $\mathbf{I} : \mathbb{R}^d \rightarrow \mathbb{R}^d$ being the identity map and $\mathbf{g} \in \mathcal{H}^d$. From the particle point of view, SVGD starts with an initial particle $\boldsymbol{\theta}_0 \sim \mu_0$ and evolves it according to the gradient dynamics, also known as the mean-field characteristic flow [33],

$$\dot{\boldsymbol{\theta}}_t = -\nabla J_{\mu_t}(\mathbf{0})(\boldsymbol{\theta}_t), \quad (6)$$

where μ_t denotes the density of $\boldsymbol{\theta}_t$ at time $t \geq 0$. The gradient $\nabla J_\mu(\mathbf{0})$ can be computed using the following relation derived in [32]

$$\nabla J_\mu(\mathbf{0})(\boldsymbol{\theta}) = -\mathbb{E}_{\mathbf{z} \sim \mu} \left[K(\mathbf{z}, \boldsymbol{\theta}) \nabla \log \pi^{(L)}(\mathbf{z}) + \nabla_1 K(\mathbf{z}, \boldsymbol{\theta}) \right], \quad (7)$$

where ∇_1 denotes the gradient with respect to the first argument. The density μ_t is the solution of the nonlinear Fokker-Planck equation corresponding to the particle evolution (6)

$$\partial_t \mu_t(\boldsymbol{\theta}) = -\nabla \cdot \left(\mu_t(\boldsymbol{\theta}) \mathbb{E}_{\mathbf{z} \sim \mu_t} \left[K(\mathbf{z}, \boldsymbol{\theta}) \nabla \log \pi^{(L)}(\mathbf{z}) + \nabla_1 K(\mathbf{z}, \boldsymbol{\theta}) \right] \right). \quad (8)$$

Much of the analysis of SVGD revolves around understanding the solution μ_t to the, potentially high-dimensional, nonlinear PDE (8). One key result that arises due to the gradient flow dynamics (8) is that the KL divergence $\text{KL}(\mu_t \parallel \pi^{(L)})$ converges to zero and it was shown in [31, Theorem 3.4] that for a solution μ_t of (8) with $\text{KL}(\mu_0 \parallel \pi^{(L)}) < \infty$, it holds that

$$\frac{d}{dt} \text{KL}(\mu_t \parallel \pi^{(L)}) = -\mathbb{D}(\mu_t \parallel \pi^{(L)})^2, \quad (9)$$

where

$$\mathbb{D}(\mu \parallel \nu) = \max_{\mathbf{g} \in \mathcal{H}^d} \left\{ \mathbb{E}_{\boldsymbol{\theta} \sim \mu} [\nabla \log \nu(\boldsymbol{\theta})^\top \mathbf{g}(\boldsymbol{\theta}) + \nabla \cdot \mathbf{g}(\boldsymbol{\theta})] : \|\mathbf{g}\|_{\mathcal{H}} \leq 1 \right\}$$

is the Stein discrepancy, guaranteeing that the KL divergence from the target decreases monotonically. The result (9) provides motivation for considering a monotone convergence behavior as in Assumption 5 later. The Stein discrepancy $\mathbb{D}(\mu \parallel \nu) = 0$ if $\mu = \nu$, but the converse may only be valid if the space \mathcal{H} is sufficiently rich and can otherwise result in a biased estimate of the quantity of interest (2).

Remark 1. *There is a strong connection between SVGD and the unadjusted Langevin algorithm [23] in the sense that the Langevin algorithm evolves a density that minimizes the KL divergence in the Wasserstein metric as opposed to a SVGD that uses a kernelized Wasserstein metric [10].*

2.3 Multilevel Stein variational gradient descent

The work [3] introduced a multilevel variant of SVGD and showed that one can achieve a cost complexity reduction by integrating the continuous-time mean-field flow (6) with successively more accurate and more expensive-to-evaluate low-fidelity densities $\pi^{(1)}, \dots, \pi^{(L)}$ as opposed to integrating only with respect to the high-fidelity density $\pi^{(L)}$. The analysis in [3] of the cost complexity relied on the following assumptions.

Assumption 1. The costs c_ℓ of integrating (8) with target density $\pi^{(\ell)}$ for a unit time interval are bounded as

$$c_\ell \leq c_0 s^{\gamma_\ell}, \quad \ell \in \mathbb{N},$$

with constants $c_0, \gamma > 0$ independent of ℓ and $s > 1$.

Assumption 2. There exists $\alpha, k_0, k_1 > 0$ independent of ℓ such that $\text{KL}(\mu_0 \parallel \pi^{(\ell)}) \leq k_0$ for all $\ell \in \mathbb{N}$ and

$$\text{KL}(\pi^{(\ell)} \parallel \pi) \leq k_1 s^{-\alpha_\ell}, \quad \ell \in \mathbb{N},$$

where s is the same constant independent of ℓ as in Assumption 1 and μ_0 is the initial distribution.

Assumption 3. There exists a rate $\lambda > 0$ such that for any initial distribution ν_0

$$\text{KL}(\nu_t \parallel \pi^{(\ell)}) \leq e^{-\lambda t} \text{KL}(\nu_0 \parallel \pi^{(\ell)}), \quad \ell \in \mathbb{N},$$

holds, where ν_t solves the mean-field SVGD equation (8) at time t .

Single-level SVGD derives an approximation μ^{SL} such that $d_{\text{Hell}}(\mu^{\text{SL}}, \pi) \leq \epsilon$, by selecting a high-fidelity approximation $\pi^{(L)}$ with

$$d_{\text{Hell}}(\pi^{(L)}, \pi) \leq \epsilon/2 \tag{10}$$

and then integrating (8) with respect to $\pi^{(L)}$ for time $T_{\text{SL}}(\epsilon)$

$$T_{\text{SL}}(\epsilon) = \min \left\{ t \geq 0 : d_{\text{Hell}}(\mu_t, \pi^{(L)}) \leq \frac{\epsilon}{2} \right\}. \tag{11}$$

This leads to the cost of continuous-time single-level SVGD

$$c_{\text{SL}}(\epsilon) = c_{L(\epsilon)} T_{\text{SL}}(\epsilon),$$

where the cost $c_{L(\epsilon)}$ depends on ϵ through the level L that is selected such that (10) holds. In the remainder of this manuscript, for brevity, we drop the explicit dependence $L = L(\epsilon)$ and similarly $T_{\text{SL}} = T_{\text{SL}}(\epsilon)$ when ϵ is fixed. The following upper bound for the cost complexity of single-level SVGD was derived in [3, Proposition 2].

Proposition 1. If Assumptions 1–3 hold, then the costs of continuous-time single-level SVGD to obtain μ^{SL} with

$$d_{\text{Hell}}(\mu^{\text{SL}}, \pi) \leq \epsilon,$$

is bounded as

$$c_{\text{SL}}(\epsilon) \leq \frac{2c_0 s^\gamma}{\lambda} \left(\frac{\sqrt{2k_1}}{\epsilon} \right)^{2\gamma/\alpha} \log \left(\frac{\sqrt{\text{KL}(\mu_0 \parallel \pi^{(L)})}}{\sqrt{2}\epsilon} \right), \tag{12}$$

with high-fidelity level

$$L = \left\lceil \frac{1}{2\alpha} \log_s \left(\frac{\sqrt{2k_1}}{\epsilon} \right) \right\rceil. \tag{13}$$

From (12), a higher initial KL divergence $\text{KL}(\mu_0 \parallel \pi^{(L)})$ or a slower convergence rate (small λ) for SVGD will result in a larger cost complexity to obtain the single-level SVGD approximation of $\pi^{(L)}$. In contrast to single-level SVGD, the MLSVD method introduced in [3] first integrates with respect to the cheapest and least accurate lowest fidelity density $\pi^{(1)}$ for time $T_1 > 0$ to obtain density $\mu_{T_1}^{(1)}$, which serves as an initial density for the next level and so on until the highest level L is reached. For $\ell = 1, \dots, L$, let $\mu_{T_\ell}^{(\ell)}$ be the

solution of (8), with the low-fidelity density $\pi^{(\ell)}$ replacing the target π , at time T_ℓ with initial density $\mu_{T_{\ell-1}}^{(\ell-1)}$ where the times T_ℓ are given by

$$T_\ell = \min \left\{ t \geq 0 : \text{KL} \left(\mu_t^{(\ell)} \parallel \pi^{(\ell)} \right) \leq \frac{\epsilon_\ell^2}{2} \right\}, \quad (14)$$

where $\epsilon_1 \geq \epsilon_2 \geq \dots \geq \epsilon_L$ and $\epsilon_L \leq \epsilon$ is a sequence of tolerances. Then, the continuous-time MLSVGD approximation is defined as

$$\mu^{\text{ML}} = \mu_{T_L}^{(L)},$$

which gives the cost of MLSVGD as

$$c_{\text{ML}}(\epsilon) = \sum_{\ell=1}^L c_\ell T_\ell,$$

where both L and T_ℓ will depend on ϵ . Since the KL divergence does not satisfy the triangle inequality, the following assumption for MLSVGD ensures that the KL divergence between levels converges as well, which is different from Assumption 2.

Assumption 4. *There exists a constant $k_2 > 0$ independent of ℓ such that $\text{KL}(\pi^{(\ell-1)} \parallel \pi^{(\ell)}) \leq k_2 s^{-\alpha}$, where α is the same rate as in Assumption 2.*

With these additional assumptions one can derive the cost complexity for MLSVGD [3, Proposition 4] below.

Proposition 2. *If Assumptions 1–4 hold and $R_\ell \leq k_3 s^{-\alpha_\ell}$ and*

$$\epsilon_\ell = \sqrt{2k_1} s^{-\alpha_\ell/2},$$

where

$$R_\ell = \int_{\mathbb{R}^d} \left(\mu_{T_{\ell-1}}^{(\ell-1)}(\boldsymbol{\theta}) - \pi^{(\ell-1)}(\boldsymbol{\theta}) \right) \log \left(\frac{\pi^{(\ell-1)}(\boldsymbol{\theta})}{\pi^{(\ell)}(\boldsymbol{\theta})} \right) d\boldsymbol{\theta}, \quad (15)$$

then the costs of continuous-time MLSVGD to have $d_{\text{Hell}}(\mu^{\text{ML}}, \pi) \leq \epsilon$ can be bounded as

$$c_{\text{ML}}(\epsilon) \leq \frac{c_0 s^{2\gamma}}{\lambda \gamma \log(s)} \log \left(s^\alpha + \frac{k_2 + k_3}{k_1} \right) \left(\frac{\sqrt{2k_1}}{\epsilon} \right)^{2\gamma/\alpha}. \quad (16)$$

The cost complexity of MLSVGD scales at most as $\mathcal{O}(\epsilon^{-2\gamma/\alpha})$, whereas the cost complexity for single-level SVGD has an additional $\log \epsilon^{-1}$ factor. Furthermore, the bound (16) is independent of the KL divergence of the initial density μ_0 and instead only depends on the constant k_2 that measures the KL divergence between successive levels.

3 Further analysis of MLSVGD

We now extend the analysis of MLSVGD to apply in settings where SVGD exhibits other convergence rates than exponential ones, which greatly extends the scope of the analysis because SVGD achieves exponential convergence rates in fairly limited settings [16]. Additionally, the new analysis also applies to the discrete-time formulation of SVGD, which is closer to what is used in practice, instead of only the continuous-time formulation as in [3].

In Section 3.1 we extend the results of [3] for continuous-time MLSVGD and SVGD by relaxing Assumption 3 to a more general rate of convergence. Additionally, in Section 3.2 we show that the analysis from Section 3.1 is also applicable in the discrete-time setting where MLSVGD and SVGD approximations are updated according to an explicit Euler time integration scheme. Finally, in Section 3.3, we show that the assumptions required by the new analysis hold in typically settings of Bayesian inverse problems.

3.1 Continuous-time MLSVGD with general convergence rate

Following from Equation (9) we know that the KL divergence decreases monotonically along the flow (8) that continuous-time MLSVGD and continuous-time SVGD integrate. However, the KL divergence does not necessarily decrease at an exponential rate as required by Assumption 3 used in the analysis of MLSVGD introduced in [3], see Section 2.3. We now consider a relaxed assumption on the convergence rate.

Assumption 5. *There exists a decreasing function $r : [0, \infty) \rightarrow [0, 1]$ such that $r(0) = 1$, $\lim_{t \rightarrow \infty} r(t) = 0$, and for an initial distribution ν_0*

$$\text{KL}(\nu_t \parallel \pi^{(\ell)}) \leq r(t) \text{KL}(\nu_0 \parallel \pi^{(\ell)}), \quad \ell \in \mathbb{N},$$

holds, where ν_t is the solution of the mean-field SVGD equation (8) at time t .

Note that from (9), Assumption 5 is guaranteed to hold for any particular $\ell \in \mathbb{N}$ and initial distribution ν_0 . Assumption 5 requires that the convergence rate is uniform across all levels and initial distributions ν_0 . In the case where r is not invertible due to a discontinuity, we define

$$r^{-1}(\epsilon) = \min \{t \in [0, \infty) : r(t) \leq \epsilon\}. \quad (17)$$

We now derive a result analogous to Proposition 1.

Proposition 3. *If Assumptions 1,2,5 hold, then the costs of continuous-time SVGD to obtain μ^{SL} with*

$$d_{\text{Hell}}(\mu^{\text{SL}}, \pi) \leq \epsilon,$$

is bounded as

$$c_{\text{SL}}(\epsilon) \leq c_0 s^{\gamma L} T_{\text{SL}} \leq 2c_0 s^{\gamma} (2k_1)^{\gamma/\alpha} r^{-1} \left(\frac{\epsilon^2}{2 \text{KL}(\mu_0 \parallel \pi^{(L)})} \right) \epsilon^{-2\gamma/\alpha}. \quad (18)$$

Proof. By the triangle inequality for the Hellinger distance we have that

$$d_{\text{Hell}}(\mu^{\text{SL}}, \pi) \leq d_{\text{Hell}}(\mu^{\text{SL}}, \pi^{(L)}) + d_{\text{Hell}}(\pi^{(L)}, \pi),$$

so we will bound both of these terms independently by $\epsilon/2$. By inequality (5), it is sufficient to bound the KL divergence because

$$d_{\text{Hell}}(\mu^{\text{SL}}, \pi^{(L)}) \leq \sqrt{\frac{\text{KL}(\mu^{\text{SL}} \parallel \pi^{(L)})}{2}}, \quad (19)$$

and similarly for $d_{\text{Hell}}(\pi^{(L)}, \pi)$. By Assumption 2 choose L to be

$$L = \left\lceil \frac{1}{\alpha} \log_s \left(\frac{2k_1}{\epsilon^2} \right) \right\rceil \leq \frac{1}{\alpha} \log_s \left(\frac{2k_1}{\epsilon^2} \right) + 1, \quad (20)$$

so that

$$d_{\text{Hell}}(\pi^{(L)}, \pi) \leq \sqrt{\frac{\text{KL}(\pi^{(L)} \parallel \pi)}{2}} \leq \sqrt{\frac{k_1 s^{-\alpha L}}{2}} \leq \frac{\epsilon}{2}. \quad (21)$$

The time needed to integrate with SVGD to achieve $d_{\text{Hell}}(\mu^{\text{SL}}, \pi^{(L)}) \leq \epsilon/2$ is

$$T_{\text{SL}} = \min \left\{ t \geq 0 : d_{\text{Hell}}(\mu_t, \pi^{(L)}) \leq \frac{\epsilon}{2} \right\}.$$

Again by inequality (5),

$$T_{\text{SL}} \leq \min \left\{ t \geq 0 : \text{KL} \left(\mu_t \parallel \pi^{(L)} \right) \leq \frac{\epsilon^2}{2} \right\}.$$

Now by Assumption 5, the rate function r is invertible, or by applying the definition (17) of r^{-1} , and the time needed to integrate with SVGD to achieve $d_{\text{Hell}}(\mu^{\text{SL}}, \pi^{(L)}) \leq \epsilon/2$ is bounded as

$$T_{\text{SL}} \leq r^{-1} \left(\frac{\epsilon^2}{2\text{KL}(\mu_0 \parallel \pi^{(L)})} \right). \quad (22)$$

With Assumption 1, the total cost to integrate until time T_{SL} at level L is therefore bounded as

$$c_{\text{SL}}(\epsilon) \leq c_0 s^{\gamma L} T_{\text{SL}} \leq 2c_0 s^{\gamma} (2k_1)^{\gamma/\alpha} r^{-1} \left(\frac{\epsilon^2}{2\text{KL}(\mu_0 \parallel \pi^{(L)})} \right) \epsilon^{-2\gamma/\alpha}.$$

□

As in Proposition 1 we see that the cost complexity depends on the tolerance ϵ , the KL divergence of the initial distribution μ_0 from the high-fidelity density $\pi^{(L)}$, as well as the SVGD convergence rate. Because the rate function r is decreasing, its inverse r^{-1} is also decreasing and so a larger initial KL divergence will require a longer integration time. We also derive a new cost complexity for the more general convergence rate for continuous-time MLSVGd in the following proposition.

Proposition 4. *If Assumptions 1, 2, 4, and 5 hold and $R_\ell \leq k_3 s^{-\alpha\ell}$, then by setting $\epsilon_\ell = \sqrt{2k_1} s^{-\alpha\ell/2}$ for $\ell = 1, \dots, L$, the costs of continuous-time MLSVGd to have $d_{\text{Hell}}(\mu^{\text{ML}}, \pi) \leq \epsilon$ can be bounded as*

$$c_{\text{ML}}(\epsilon) \leq \frac{c_0 s^{2\gamma} (2k_1)^{\gamma/\alpha}}{s^\gamma - 1} r^{-1} \left(\frac{1}{s^\alpha + (k_2 + k_3)/k_1} \right) \epsilon^{-2\gamma/\alpha}. \quad (23)$$

Proof. As in Equation (20) in the proof of Proposition 3 we select the level L as

$$L = \left\lceil \frac{1}{\alpha} \log_s \left(\frac{2k_1}{\epsilon^2} \right) \right\rceil \leq \frac{1}{\alpha} \log_s \left(\frac{2k_1}{\epsilon^2} \right) + 1, \quad (24)$$

so that $d_{\text{Hell}}(\pi^{(L)}, \pi) \leq \epsilon/2$. Note that by setting $\epsilon_\ell = \sqrt{2k_1} s^{-\alpha\ell/2}$ for $\ell = 1, \dots, L$ in (14) we have that

$$\frac{\epsilon_L^2}{2} = k_1 s^{-\alpha L} \leq \frac{\epsilon}{2},$$

by the choice of the high-fidelity level L (20).

By Assumption 1, the total cost for MLSVGd is bounded by

$$c_{\text{ML}}(\epsilon) \leq \sum_{\ell=1}^L c_0 s^{\gamma\ell} T_\ell, \quad (25)$$

where it remains to bound the integration times T_ℓ at each level. By Assumption 5 and Equation (26), we have

$$\begin{aligned} \text{KL}(\mu_{T_\ell}^{(\ell)} \parallel \pi^{(\ell)}) &\leq r(T_\ell) \text{KL}(\mu_{T_{\ell-1}}^{(\ell-1)} \parallel \pi^{(\ell)}) \\ &= r(T_\ell) \left(\text{KL}(\mu_{T_{\ell-1}}^{(\ell-1)} \parallel \pi^{(\ell-1)}) + \text{KL}(\pi^{(\ell-1)} \parallel \pi^{(\ell)}) + R_\ell \right), \end{aligned} \quad (26)$$

giving a recursive bound on the KL divergence in terms of the KL divergence at the previous level. By the definition (14) of the integration times T_ℓ at level ℓ , we know that

$$\text{KL} \left(\mu_{T_\ell}^{(\ell)} \parallel \pi^{(\ell)} \right) \leq \frac{\epsilon_\ell^2}{2}, \quad (27)$$

is satisfied for each level $\ell = 1, \dots, L$. Using (27) at level $\ell - 1$ gives

$$\text{KL} \left(\mu_{T_\ell}^{(\ell)} \parallel \pi^{(\ell)} \right) \leq r(T_\ell) \left(\frac{\epsilon_{\ell-1}^2}{2} + \text{KL} \left(\pi^{(\ell-1)} \parallel \pi^{(\ell)} \right) + R_\ell \right). \quad (28)$$

Note that by (27) we know that the left-hand-side of (28) is guaranteed to be bounded above by $\epsilon_\ell^2/2$, but the same is not necessarily true for the right-hand-side which is an upper bound. Instead define T'_ℓ as

$$T'_\ell = \min \left\{ t \geq 0 : r(t) \left(\frac{\epsilon_{\ell-1}^2}{2} + \text{KL} \left(\pi^{(\ell-1)} \parallel \pi^{(\ell)} \right) + R_\ell \right) \leq \frac{\epsilon_\ell^2}{2} \right\}, \quad (29)$$

for each level $\ell = 1, \dots, L$, which is finite by the assumption that $r(t) \rightarrow 0$ (Assumption 5). By (28) and because r is monotonically decreasing we know that $T_\ell \leq T'_\ell$. Solving directly gives

$$T'_\ell \leq r^{-1} \left(\frac{\epsilon_\ell^2}{\epsilon_{\ell-1}^2 + 2\text{KL} \left(\pi^{(\ell-1)} \parallel \pi^{(\ell)} \right) + 2R_\ell} \right). \quad (30)$$

We now use the fact that r^{-1} is decreasing as well as Assumption 4 and the assumption that $R_\ell \leq k_3 s^{-\alpha\ell}$ to bound

$$r^{-1} \left(\frac{\epsilon_\ell^2}{\epsilon_{\ell-1}^2 + 2\text{KL} \left(\pi^{(\ell-1)} \parallel \pi^{(\ell)} \right) + 2R_\ell} \right) \leq r^{-1} \left(\frac{\epsilon_\ell^2}{\epsilon_{\ell-1}^2 + 2k_2 s^{-\alpha\ell} + 2k_3 s^{-\alpha\ell}} \right).$$

Therefore, by substituting $\epsilon_\ell = \sqrt{2k_1} s^{-\alpha\ell/2}$ (and similarly for $\epsilon_{\ell-1}$) we can bound T'_ℓ , and hence T_ℓ , with

$$T_\ell \leq r^{-1} \left(\frac{2k_1 s^{-\alpha\ell}}{2k_1 s^\alpha s^{-\alpha\ell} + 2k_2 s^{-\alpha\ell} + 2k_3 s^{-\alpha\ell}} \right).$$

Simplifying gives the bound

$$T_\ell \leq r^{-1} \left(\frac{1}{s^\alpha + (k_2 + k_3)/k_1} \right), \quad (31)$$

which is independent of the tolerance ϵ . The total cost can now be bounded by

$$c_{\text{ML}}(\epsilon) \leq \sum_{\ell=1}^L c_0 s^{\gamma\ell} r^{-1} \left(\frac{1}{s^\alpha + (k_2 + k_3)/k_1} \right), \quad (32)$$

which we may again compute explicitly

$$\begin{aligned} c_{\text{ML}}(\epsilon) &\leq c_0 s^{\gamma} r^{-1} \left(\frac{1}{s^\alpha + (k_2 + k_3)/k_1} \right) \frac{s^{\gamma L} - 1}{s^{\gamma} - 1} \\ &\leq c_0 s^{\gamma} r^{-1} \left(\frac{1}{s^\alpha + (k_2 + k_3)/k_1} \right) \frac{s^{\gamma L}}{s^{\gamma} - 1}, \end{aligned} \quad (33)$$

and we have again added 1 in the numerator of the last term for convenience. Substituting the upper bound (20) on the level L and simplifying terms gives the final upper bound on the improved cost complexity of the continuous-time MLSVD approximation μ^{ML}

$$c_{\text{ML}}(\epsilon) \leq \frac{c_0 s^{2\gamma} (2k_1)^{\gamma/\alpha}}{s^{\gamma} - 1} r^{-1} \left(\frac{1}{s^\alpha + (k_2 + k_3)/k_1} \right) \epsilon^{-2\gamma/\alpha}. \quad (34)$$

□

By setting $r(t) = e^{-\lambda t}$ as in Assumption 3, one can recover the cost complexities stated in Section 2.3. More importantly, notice that now in (23) the bound on the cost complexity is actually independent of the rate of convergence for SVGD other than a constant multiplicative factor. Thus, when compared to (18), if SVGD is slow to converge then the continuous-time MLSVDG can spend most of the integration time at the lower levels, which may be orders of magnitude faster to integrate, in order to find a good initial density for integrating with respect to the highest level L and achieve potentially large speedups. In contrast, if SVGD converges quickly then the low-fidelity densities will be less beneficial and both costs will be comparable.

3.2 Discrete-time MLSVDG with general convergence rates

The analysis presented so far, as well as the one introduced in [3], only applies to continuous-time solutions of (8) where one can sample exactly by integrating along the characteristic flow (6). In this section, we consider the discrete-time formulations of SVGD and MLSVDG where the characteristic flow (8) is not integrated exactly but instead is numerically approximated.

3.2.1 Discrete-time SVGD

We apply the explicit Euler method to the flow (6) to obtain

$$\boldsymbol{\theta}_{\tau+1} = \boldsymbol{\theta}_{\tau} - \delta \mathbf{g}_{\tau}(\boldsymbol{\theta}_{\tau}), \quad \mathbf{g}_{\tau} = \nabla J_{\mu_{\tau}}(\mathbf{0}), \quad (35)$$

with step size $\delta > 0$. The update \mathbf{g}_{τ} is obtained with

$$\mu_{\tau+1} = (\mathbf{I} - \delta \mathbf{g}_{\tau})_{\#} \mu_{\tau},$$

for iterations $\tau = 0, 1, 2, \dots$. The work [31, Theorem 3.3] showed that an analogous equation to (9) holds for the discrete-time SVGD,

$$\text{KL}(\mu_{\tau+1} \parallel \pi^{(L)}) \leq \text{KL}(\mu_{\tau} \parallel \pi^{(L)}) - \delta(1 - \delta B) \mathbb{D}(\mu_{\tau} \parallel \pi^{(L)})^2, \quad (36)$$

where the constant B depends on the kernel K and the target density $\pi^{(L)}$. Moreover, [31, Theorem 3.3] showed that when the step size δ decreases sufficiently fast as the iterations increase, the sequence of measures $(\mu_{\tau})_{\tau=0}^{\infty}$ minimizes the KL divergence from the target $\pi^{(L)}$.

3.2.2 Discrete-time MLSVDG

In this section, we extend the results of Propositions 3 and 4 to the discrete-time setting where we update a particle $\boldsymbol{\theta}_{\tau}$ with a sequence of transport maps as in (35). Since we are no longer integrating a continuous-time flow we have to replace Assumption 1 with a discrete-time version that reflects the cost of a single evaluation of the gradient log density.

Assumption 6. *The costs c_{ℓ} of evaluating the gradient of the log density $\nabla \log \pi^{(\ell)}(\boldsymbol{\theta})$ at any point $\boldsymbol{\theta} \in \Theta$, are bounded as*

$$c_{\ell} \leq c_0 s^{\gamma \ell}, \quad \ell \in \mathbb{N},$$

with constants $c_0, \gamma > 0$ and $s > 1$ independent of ℓ .

We also need to replace Assumption 5 with an assumption that holds for discrete-time rate functions with domain $\mathbb{N}_0 = \{0\} \cup \mathbb{N}$ instead of \mathbb{R} : Just as in (9) where the KL divergence is guaranteed to be decreasing for solutions μ_t to (8), Equation 36 guarantees that for a small enough time step δ , the sequence of densities $(\mu_{\tau})_{\tau=1}^{\infty}$ will also decrease the KL divergence monotonically.

Assumption 7. *There exists a decreasing function $r : \mathbb{N}_0 \rightarrow [0, 1]$ such that $r(0) = 1$, $\lim_{\tau \rightarrow \infty} r(\tau) = 0$, and for any initial distribution ν_0*

$$\text{KL}(\nu_\tau \parallel \pi^{(\ell)}) \leq r(\tau) \text{KL}(\nu_0 \parallel \pi^{(\ell)}), \quad \ell \in \mathbb{N},$$

holds, where ν_τ evolves according to the discrete-time SVGD update (35).

We select the high-fidelity level L analogously to the continuous-time case so that $d_{\text{Hell}}(\pi^{(L)}, \pi) \leq \epsilon/2$ and define the discrete-time single-level SVGD approximation μ^{SL} as the solution $\mu_{T_{\text{SL}}}$ after updating (35) for T_{SL} iterations where

$$T_{\text{SL}} = \min \left\{ \tau \in \mathbb{N}_0 : d_{\text{Hell}}(\mu_\tau, \pi^{(L)}) \leq \frac{\epsilon}{2} \right\}.$$

We define the discrete-time MLSVGD approximation similarly. Since the rate function r is now a function on the non-negative integers it may no longer have an inverse defined on $[0, 1]$. Instead we define

$$r^{-1}(\epsilon) = \min \{ \tau \in \mathbb{N}_0 : r(\tau) \leq \epsilon \}.$$

We now can state the cost complexity bounds for SVGD and MLSVGD.

Proposition 5. *If Assumptions 6, 2, 7 hold, then the costs of discrete-time SVGD to obtain μ^{SL} with*

$$d_{\text{Hell}}(\mu^{\text{SL}}, \pi) \leq \epsilon$$

is bounded as

$$c_{\text{SL}}(\epsilon) \leq 2c_0 s^\gamma \left(\frac{\sqrt{2k_1}}{\epsilon} \right)^{2\gamma/\alpha} r^{-1} \left(\frac{\epsilon^2}{2\text{KL}(\mu_0 \parallel \pi^{(L)})} \right). \quad (37)$$

Proof. Analogous to the continuous-time case. □

Proposition 6. *If Assumptions 1, 2, 4, and 7 hold and $R_\ell \leq k_3 s^{-\alpha\ell}$, then the costs of discrete-time MLSVGD to have $d_{\text{Hell}}(\mu^{\text{ML}}, \pi) \leq \epsilon$ can be bounded as*

$$c_{\text{ML}}(\epsilon) \leq \frac{c_0 s^{2\gamma}}{\gamma \log(s)} r^{-1} \left(\left[s^\alpha + \frac{k_2 + k_3}{k_1} \right]^{-1} \right) \left(\frac{\sqrt{2k_1}}{\epsilon} \right)^{2\gamma/\alpha}. \quad (38)$$

Proof. Analogous to the continuous-time case. □

3.3 Cost complexity for Bayesian inverse problems

We now show that the results from both Sections 3.1 and 3.2 are applicable in typical Bayesian inverse problem settings. Recall that typically in Bayesian inverse problems, the sequence of posterior distributions $(\pi^{(\ell)})$ is obtained via a sequence of approximate parameter-to-observable maps $(G^{(\ell)})_{\ell=1}^\infty$ with $G^{(\ell)}(\theta) \rightarrow G(\theta)$ pointwise for every $\theta \in \Theta$, so that the sequence of densities $(\pi^{(\ell)})$ converges pointwise as well. The following assumption on the parameter-to-observable maps ensures that the KL divergences of the densities converges as required in Assumptions 2 and 4.

Assumption 8. *The error of the approximate parameter-to-observable $G^{(\ell)}$ map at level $\ell \geq 1$ is bounded by*

$$\|G(\theta) - G^{(\ell)}(\theta)\|_{L^2(\pi_0)} \leq b_0 s^{-\alpha\ell}, \quad (39)$$

where $\alpha, b_0 > 0$ and $s > 1$ are constants with s the same as in Assumption 1 and $\|\cdot\|_{L^2(\pi_0)}$ is the L^2 norm over π_0 .

We also make the following assumption to ensure that the SVGD approximations $\mu_{T_\ell}^{(\ell)}$ remain absolutely continuous at each level with respect to the prior density π_0 in order to control the remainders R_ℓ defined in (15).

Assumption 9. *There exists a constant $b_3 > 0$ independent of ℓ such that*

$$\mu_{T_\ell}^{(\ell)}(\boldsymbol{\theta}) \leq b_3 \pi_0(\boldsymbol{\theta}), \quad \boldsymbol{\theta} \in \Theta, \quad (40)$$

for all $\ell \geq 1$.

Under these additional assumptions, Theorem 6 in [3] showed that the low-fidelity densities $\pi^{(\ell)}$ satisfy the assumptions from Section 2.3 and therefore Proposition 2 applies.

Theorem 1. *If Assumptions 1, 5 (or equivalently Assumption 6 and 7 in the discrete-time setting), and 9 hold and Assumption 8 holds with $\psi(\ell) = b_0 s^{-\alpha\ell}$, then Assumptions 2 and 4 hold and thus the cost complexity to find μ^{ML} with $d_{\text{Hell}}(\mu^{\text{ML}}, \pi) \leq \epsilon$ is given by*

$$c_{\text{ML}}(\epsilon) \leq \frac{c_0 s^{2\gamma} (2C b_0)^{\gamma/\alpha}}{s^\gamma - 1} r^{-1} \left(\frac{1}{(1 + s^\alpha) \left(2 + \frac{b_1 b_2 + b_3}{2C} \right) - 1} \right) \epsilon^{-2\gamma/\alpha}, \quad (41)$$

where the constants b_1, b_2 are independent of ϵ .

Proof. By overloading the notation for r we consider the proofs for both the continuous-time and discrete-time cases simultaneously. Both proofs are analogous to the proof of [3, Theorem 6] with r^{-1} replacing $\frac{1}{\lambda} \log$ (see Assumption 3). \square

The asymptotic scaling of the computational complexity for MLSVGd (either discrete-time or continuous-time) is independent of the rate at which SVGd converges. Both the more general rate in Assumption 5 and the analysis in the discrete-time setting help bridge the gap from the theory presented in [3] and the practical realm where an ensemble of particles are updated according to Equation 47.

4 Numerical example: Ice sheet modeling of the Arolla glacier

To demonstrate the applicability and performance of MLSVGd, we formulate and solve an inverse problem governed by a Stokes ice sheet model. In particular, we infer the basal sliding coefficient field from pointwise surface velocity observations. The problem formulation and adjoint-based derivatives computation follows the work in [41]. The numerical computations are carried out in Python using FEniCS [1] and hippylib [43, 44, 45, 25]. All reported runtimes were measured on Intel Xeon Platinum 8268 24C 205W 2.9GHz Processor. The computation of the gradients $\nabla \log \pi^{(\ell)}(\boldsymbol{\theta}_t^{[j]})$ was parallelized over 32 cores.

4.1 Nonlinear Stokes forward model

For the numerical studies, we use an ice sheet model problem that uses the Arolla (Haut Glacier d’Arolla) geometry and setup from the ISMIP-HOM benchmark collection [35]. That is, the glacier is considered a sliding mass of ice whose velocity is determined primarily by the force of gravity and the friction against the underlying rock. The ice flow is modeled as a non-Newtonian, viscous, incompressible fluid. The velocity field \mathbf{u} over the domain $\Omega \subset \mathbb{R}^2$, as shown in Figure 1, is governed by the following Stokes equations

$$\begin{aligned} \nabla \cdot \mathbf{u} &= 0, & \text{in } \Omega, \\ -\nabla \cdot \boldsymbol{\sigma}_u &= \rho \mathbf{g}, & \text{in } \Omega. \end{aligned} \quad (42)$$

The boundary conditions along the top and bottom of the glacier are given as

$$\begin{aligned} \mathbf{n}^\top (\boldsymbol{\sigma}_u \mathbf{n} + \lambda \mathbf{u}) &= 0, & \text{on } \Gamma_b, \\ \mathbf{T} \boldsymbol{\sigma}_u \mathbf{n} + \exp(\beta) \mathbf{T} \mathbf{u} &= \mathbf{0}, & \text{on } \Gamma_b, \\ \boldsymbol{\sigma}_u \mathbf{n} &= \mathbf{0}, & \text{on } \Gamma_t. \end{aligned} \quad (43)$$

The density of the ice is $\rho = 910$ [kg/m³] and the downwards gravitational force is $\mathbf{g} = (0, -9.81)$ [m/s²]. For the boundary conditions, Γ_b represents the bottom part of the domain where the ice slides across the bedrock and Γ_t represents the top part of the domain; see Figure 1. The vector \mathbf{n} represents the outward unit normal vector and $\mathbf{T} = \mathbf{I} - \mathbf{n}\mathbf{n}^\top$ is the tangential projection. In the first boundary condition where $\mathbf{n}^\top (\boldsymbol{\sigma}_u \mathbf{n} + \lambda \mathbf{u}) = 0$ on Γ_b we set the parameter $\lambda = 10^6$ and is meant to approximate the no out-flow condition $\mathbf{u} \cdot \mathbf{n} = 0$, which is difficult to enforce directly due to the curvature of the domain Ω . The stress tensor is

$$\boldsymbol{\sigma}_u = \boldsymbol{\tau}_u - \mathbf{I}p,$$

with pressure p and deviatoric stress tensor

$$\boldsymbol{\tau}_u = 2\eta(\mathbf{u})\dot{\boldsymbol{\epsilon}}(\mathbf{u}),$$

with effective viscosity

$$\eta(\mathbf{u}) = \frac{1}{2} A^{-\frac{1}{n}} \dot{\boldsymbol{\epsilon}} \cdot \frac{1-n}{2n} \boldsymbol{\Pi}.$$

The constants are Glen's flow law exponent $n = 3$ and the flow rate factor $A = 10^{-16}$ [Pa⁻ⁿa⁻¹] (Pascals and years, respectively). The strain rate tensor is

$$\dot{\boldsymbol{\epsilon}} = \frac{1}{2} (\nabla \mathbf{u} + \nabla \mathbf{u}^\top),$$

as well as the second invariant

$$\dot{\boldsymbol{\epsilon}} \cdot \boldsymbol{\Pi} = \frac{1}{2} \text{tr}(\dot{\boldsymbol{\epsilon}}^2),$$

where tr denotes the trace operator. The parameter of interest is the log basal sliding coefficient field $\beta : [0, 5000] \rightarrow \mathbb{R}$, which models the friction of the ice sheet across the underlying bedrock and relates tangential traction to the tangential velocity.

To solve (42), we discretize (42)–(43) using Taylor-Hood finite elements on a triangular mesh where the velocity is discretized with quadratic Lagrange elements and the pressure is discretized with linear Lagrange elements. We consider one high-fidelity model and two low-fidelity models by coarsening the mesh. The high-fidelity forward model $F^{(3)}$ ($L = 3$) maps the log basal sliding coefficient field β to the velocity field solution \mathbf{u} using 3,602 and 501 degrees of freedom for the velocity and pressure components, respectively. The coarsest low-fidelity model $F^{(1)}$ uses 448 and 73 degrees of freedom for the velocity and pressure and the second low-fidelity model $F^{(2)}$ uses 1002 and 151 degrees of freedom, respectively. To solve the discretized PDE we use a constrained Newton solver with the gradient tolerance set to 10^{-6} .

4.2 Problem setup

We are interested in inferring a discretized log basal sliding coefficient field β , which effectively determines the velocity of the ice as it slides along the bedrock. We discretize the coefficient field $\beta : [0, 5000] \rightarrow \mathbb{R}$ with a vector $\boldsymbol{\beta} \in \mathbb{R}^d$ ($d = 25$) that we aim to infer from data of the parameter-to-observable map. The parameter vector $\boldsymbol{\beta} \in \mathbb{R}^{25}$ corresponds to 25 equally-spaced pointwise evaluations of the coefficient field β throughout the domain $[0, 5000]$. In particular, let \mathcal{I}^{int} denote the interpolation operator that maps a vector $\boldsymbol{\beta} \in \mathbb{R}^{25}$ to its piecewise linear interpolant $\bar{\beta} : [0, 5000] \rightarrow \mathbb{R}$ defined at the nodes $x_i = 5000(i - 1)/24$ by $\bar{\beta}(x_i) = \beta_i$ for $i = 1, \dots, 25$. Given the piecewise linear interpolant $\bar{\beta}$, the forward models $F^{(\ell)}$ for $\ell = 1, 2, 3$

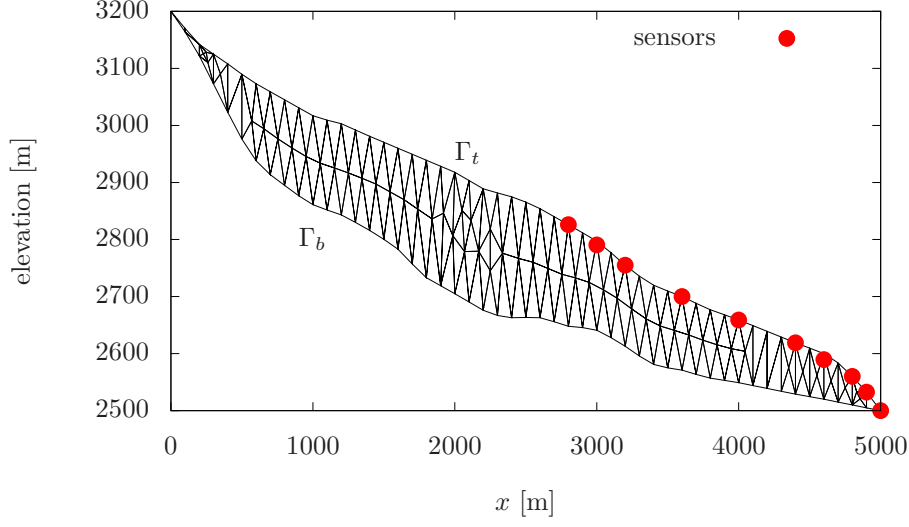


Figure 1: The domain Ω of Haut Glacier d'Arolla from the ISMIP-HOM benchmark collection [35]. The red dots represent the location of the measurements.

map the parameter to the corresponding velocity field \mathbf{u} . Finally, the observation operator \mathcal{B}^{obs} maps the solution \mathbf{u} of (42), given by the output of the forward models $F^{(\ell)}$, to a 20 dimensional vector of horizontal and vertical velocity measurements at 10 sensor locations throughout the right side of the domain along the top of the glacier as shown in 1. The full parameter-to-observable map $G^{(\ell)} : \mathbb{R}^{25} \rightarrow \mathbb{R}^{20}$ is therefore

$$G^{(\ell)} = \mathcal{B}^{\text{obs}} \circ F^{(\ell)} \circ \mathcal{I}^{\text{int}}, \quad \ell = 1, 2, 3.$$

Now consider the true parameter vector $\beta^* = [\beta_1^*, \dots, \beta_{25}^*]^\top \in \mathbb{R}^{25}$ as given by taking pointwise evaluations

$$\beta_i^* = \beta_{\text{true}}(x_i), \quad x_i = 5000(i-1)/24, \quad i = 1, \dots, 25, \quad (44)$$

where

$$\beta_{\text{true}}(x) = \log \begin{cases} 1000 + 1000 \sin\left(\frac{3\pi x}{5000}\right) + \zeta & \text{if } 0 \leq x < 2500, \\ 1000 \left(16 - \frac{x}{250}\right) + \zeta & \text{if } 2500 \leq x < 4000, \\ 1000 + \zeta & \text{if } 4000 \leq x < 5000, \end{cases}$$

and $\zeta = 10^{-6}$ is a small positive constant to ensure that the log basal coefficient field remains bounded. We generate synthetic observations $\mathbf{y} \in \mathbb{R}^{20}$ with

$$\mathbf{y} = G^{(L+1)}(\beta^*) + \boldsymbol{\eta}, \quad \boldsymbol{\eta} \sim N(\mathbf{0}, \Gamma),$$

where the noise covariance matrix Γ is diagonal with $\sigma_{\text{vertical}} = 3$ and $\sigma_{\text{horizontal}} = 18$ corresponding to the vertical and horizontal velocity measurements, respectively. Here the level $L+1$ (a further refinement of the high-fidelity mesh) is used to compute the observed data \mathbf{y} .

The prior π_0 is Gaussian with mean perturbed from the true parameters β^* and diagonal covariance matrix with variance 0.05 along each diagonal. The starting distribution for SVGD and MLSVDG is the 25-dimensional standard normal distribution. The gradients of the log posterior density are computed using

adjoints with HIPPylib [43, 44, 45]. Our quantity of interest is the mean of the posterior distribution $\mathbb{E}_{\pi^{(L)}}[\beta]$ and we compute a reference value $\hat{\beta}^{\text{Ref}}$ by using the preconditioned Crank-Nicolson (pCN) method [12]. We run 100 independent chains and use a burn-in period of 10,000 samples for each chain to obtain 10^7 total samples. The parameter in the pCN algorithm is set to 10^{-2} .

4.3 SVGD algorithm with approximate gradients

Consider an empirical measure

$$\hat{\mu}_\tau^{(N)} = \frac{1}{N} \sum_{i=1}^N \delta_{\theta_\tau^{[i]}}, \quad (45)$$

given by an ensemble of particles $\{\theta_\tau^{[i]}\}_{i=1}^N$ with $\{\theta_0^{[i]}\}_{i=1}^N \sim \mu_0$ and where $\delta_{\mathbf{x}}$ represents the Dirac-mass at \mathbf{x} . Practical SVGD implementations alternate between using the ensemble of particles $\{\theta_\tau^{[i]}\}_{i=1}^N$ at time τ to estimate the gradient (7) and using the estimated gradient to update the ensemble to obtain $\hat{\mu}_{\tau+1}$. The gradient is estimated with Monte Carlo from the current ensemble of particles as

$$\hat{\mathbf{g}}_\tau(\theta) = -\frac{1}{N} \sum_{i=1}^N K(\theta_\tau^{[i]}, \theta) \nabla \log \pi^{(L)}(\theta_\tau^{[i]}) + \nabla_1 K(\theta_\tau^{[i]}, \theta). \quad (46)$$

The SVGD algorithm then reuses the ensemble of particles and updates them according to the approximate gradient with step size δ as

$$\theta_{\tau+1}^{[j]} = \theta_\tau^{[j]} - \delta \hat{\mathbf{g}}_\tau(\theta_\tau^{[j]}), \quad j = 1, \dots, N. \quad (47)$$

Because the Hellinger distance from the high-fidelity density $\pi^{(L)}$ at iteration τ is unknown, the integration time given by (11) cannot be determined practically. Instead the stopping criteria is that the average norm of the gradient \bar{g}_τ , defined as

$$\bar{g}_\tau = \frac{1}{N} \sum_{j=1}^N \left\| \hat{\mathbf{g}}_\tau(\theta_\tau^{[j]}) \right\|,$$

decreases below the predetermined threshold ϵ . The convergence of $\hat{\mu}_\tau$ to $\pi^{(L)}$ can no longer be measured in the KL divergence because at each iteration the measure $\hat{\mu}_\tau$ is no longer absolutely continuous with respect to the target $\pi^{(L)}$. Moreover, the convergence properties as the number of particles $N \rightarrow \infty$ remains an open question.

For a practical MLSVDG algorithm, an outer loop is performed over the levels $\ell = 1, \dots, L$ with the inner loop given by the SVGD updates (47). At each intermediate level $\ell < L$ the gradients (46) are obtained by replacing the high-fidelity density $\pi^{(L)}$ with the low-fidelity density $\pi^{(\ell)}$. Again, we cannot monitor the KL divergence to the target $\pi^{(\ell)}$ at each level ℓ as required by (14). Thus, the stopping criteria for when to terminate the SVGD iterations at the current level and proceed to the next level is that the norm of the gradient \bar{g}_τ decreases below the threshold ϵ .

4.4 Numerical results

In the following we compare the performance of MLSVDG and SVGD. We run both SVGD and MLSVDG with $N = 1,000$ particles, set a step size of $\delta = 0.05$, and use a Gaussian radial basis function kernel with the bandwidth parameter set to $h = 0.1$. The bandwidth parameter is kept constant, but is comparable to the one obtained from using the median heuristic presented in [32].

4.4.1 Number of iterations and runtime of SVGD and MLSVD

Figure 2 shows that with a gradient tolerance of $\epsilon = 10^{-2}$, MLSVD achieves a speedup of a factor of five over SVGD despite requiring more iterations. Note that reducing the gradient norm below $\epsilon = 10^{-2}$ corresponds to a relative reduction of the gradient norm of more than four orders of magnitude. The results presented in Figure 2 are consistent with the numerical examples presented in [3]. The runtime improvement of MLSVD over SVGD is a result of most of the iterations being performed on the lowest fidelity model with the coarsest mesh. MLSVD quickly converges to the low-fidelity posterior $\pi^{(1)}$, which serves as a good initial distribution for the following two levels whereas SVGD requires many iterations at the high-fidelity level resulting in high computational costs. The two plots in the right column of Figure 2 show that both algorithms give accurate estimates of the quantity of interest in terms of the relative error

$$\text{rel}(\beta) = \frac{\|\beta - \hat{\beta}^{\text{Ref}}\|_2}{\|\hat{\beta}^{\text{Ref}}\|_2}, \quad (48)$$

where β is the mean of the particles and $\hat{\beta}^{\text{Ref}}$ is the reference posterior mean computed with MCMC. The results suggest that the mean of the distributions of particles $\{\theta_t^{[j]}\}_{j=1}^N$ is converging to the mean of the high-fidelity target posterior $\pi^{(L)}$.

4.4.2 Speedups

MLSVD recovers a good approximation of the parameter β^* in less than a quarter of the time compared to SVGD because the low fidelity posteriors provide a good initialization. Figure 3 compares the inferred parameter means from MLSVD and SVGD after fixed amounts of training time. After two hours MLSVD has recovered the parameters whereas SVGD has not recovered them even after eight hours. We also note that the coordinates of β corresponding to the right side of the domain are recovered much faster due to the location of the velocity observation points shown in Figure 1. Moreover, Figure 4 shows the inferred velocity field u by solving (42) with the inferred parameter mean after approximately eight hours of run time over 32 cores. We see that the velocity field obtained with the MLSVD inferred parameter mean closely matches the velocity field obtained with the ground truth reference value of the mean. On the other hand, SVGD fails to recover the correct velocity field within the same amount of time. Again we see that the left side of the domain is inaccurate due to the parameter in this region not yet being accurate. Note that the magnitude of the velocity is overestimated for SVGD which is consistent with the fact that the parameter is underestimated since the parameter controls the frictional forces to resist the downward pull of gravity.

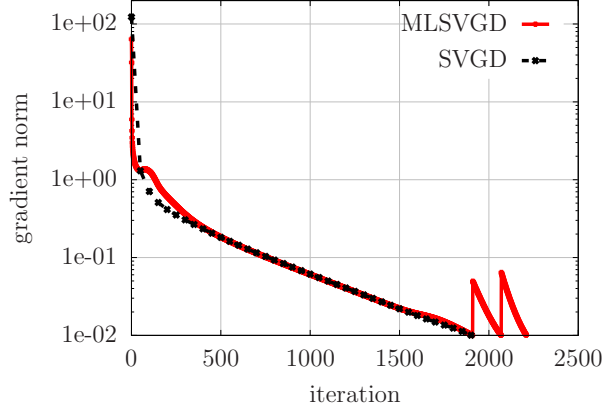
4.4.3 Sample quality

Particles obtained with SVGD tend to be evenly spread out due to the repulsive interaction between particles given by the kernel. We measure sample quality with the maximum mean discrepancy (MMD)

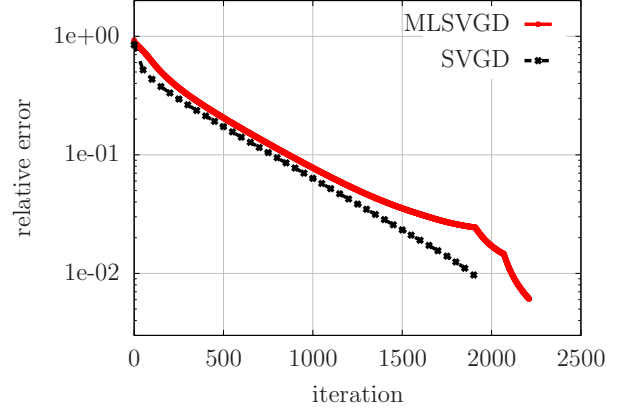
$$\text{MMD}[\mu, \nu]^2 = \sup_{\|f\|_{\mathcal{H}} \leq 1} (\mathbb{E}_{\mu}[f] - \mathbb{E}_{\nu}[f])^2,$$

where \mathcal{H} is the reproducing kernel Hilbert space with kernel K [19]. The MMD is zero if and only if the distributions $\mu = \nu$. In practice one cannot evaluate the expectations exactly, so the following estimator [19, Eq. 5] is often used instead

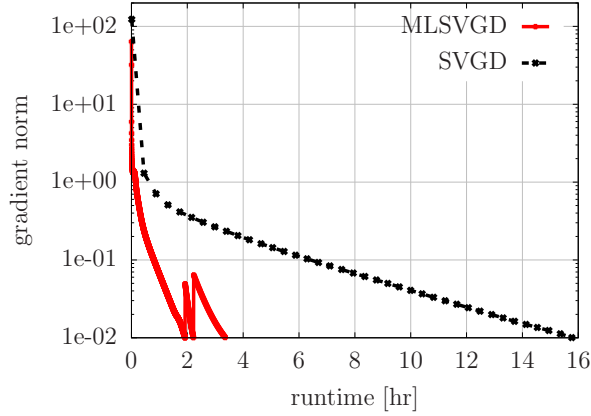
$$\begin{aligned} \widehat{\text{MMD}}(\{\mathbf{x}_i\}_{i=1}^N, \{\mathbf{y}_j\}_{j=1}^M)^2 &= \frac{1}{N^2} \sum_{i=1}^N \sum_{i'=1}^N K(\mathbf{x}_i, \mathbf{x}_{i'}) + \frac{1}{M^2} \sum_{j=1}^M \sum_{j'=1}^M K(\mathbf{y}_j, \mathbf{y}_{j'}) \\ &\quad - \frac{2}{NM} \sum_{i=1}^N \sum_{j=1}^M K(\mathbf{x}_i, \mathbf{y}_j), \end{aligned} \quad (49)$$



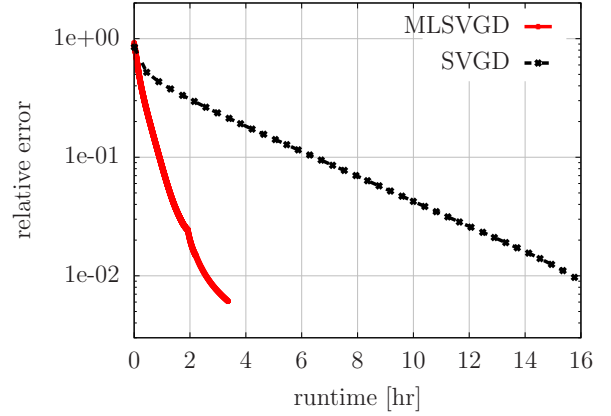
(a) gradient norm vs. iteration



(b) relative error vs. iteration



(c) gradient norm vs. runtime



(d) relative error vs. runtime

Figure 2: **(a)** The average gradient norm \bar{g}_T vs. iteration for MLSVGD and SVGD with a tolerance of $\epsilon = 10^{-2}$. **(b)** The relative error (48) of MLSVGD and SVGD compared to an MCMC reference vs. iteration. **(c)** The average gradient norms vs. the actual runtime in hours over 32 cores. **(d)** The relative error vs. actual runtime.

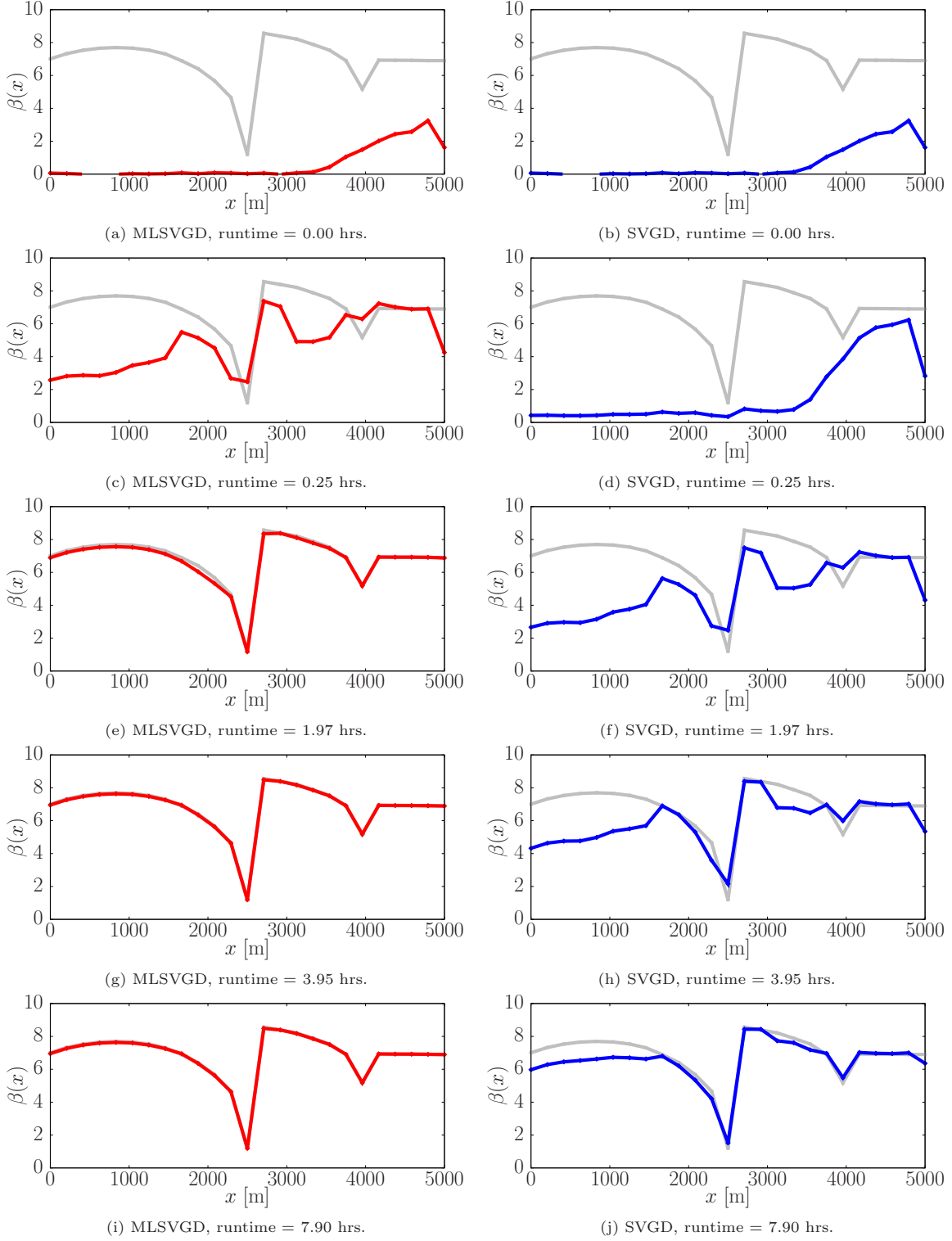
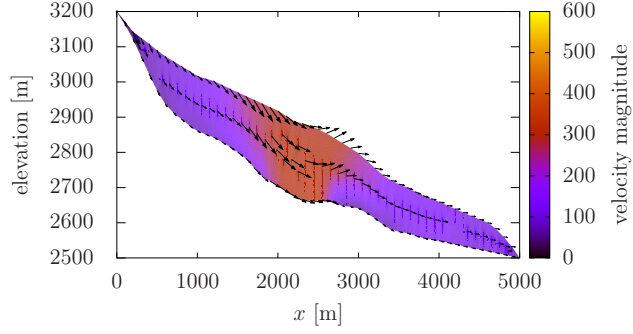
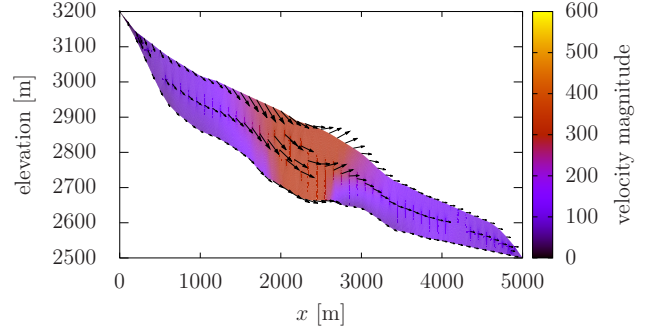


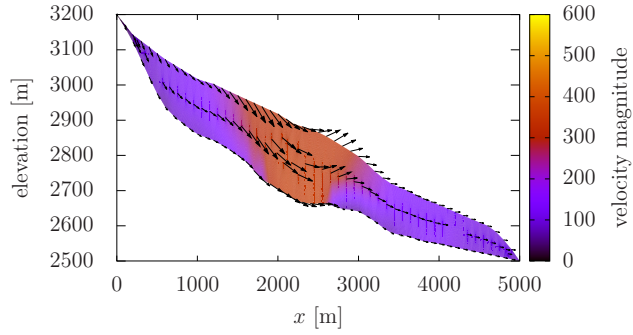
Figure 3: **(Left)** Snapshots of the MLSVGD inferred parameter mean (red) at different times. **(Right)** Snapshots of the SVGD inferred parameter mean (blue) at the same times. In each plot the solid light gray curve shows the reference value.



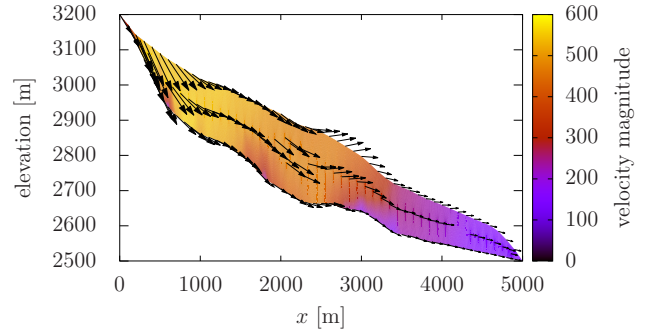
(a) true velocity field



(b) reference velocity field



(c) MLSVD inferred velocity field



(d) SVGD inferred velocity field

Figure 4: **(a)** The true velocity field given by β^* , which is defined (44). The color indicates the magnitude of the velocity in $[\text{m a}^{-1}]$ (meters per year). **(b)** The reference velocity field computed using $\hat{\beta}^{\text{Ref}}$ of the posterior mean. **(c)** The velocity field corresponding to the inferred parameters using MLSVD after eight hours. **(d)** The velocity field corresponding to the inferred parameters using SVGD with equivalent costs as MLSVD (eight hours of runtime).

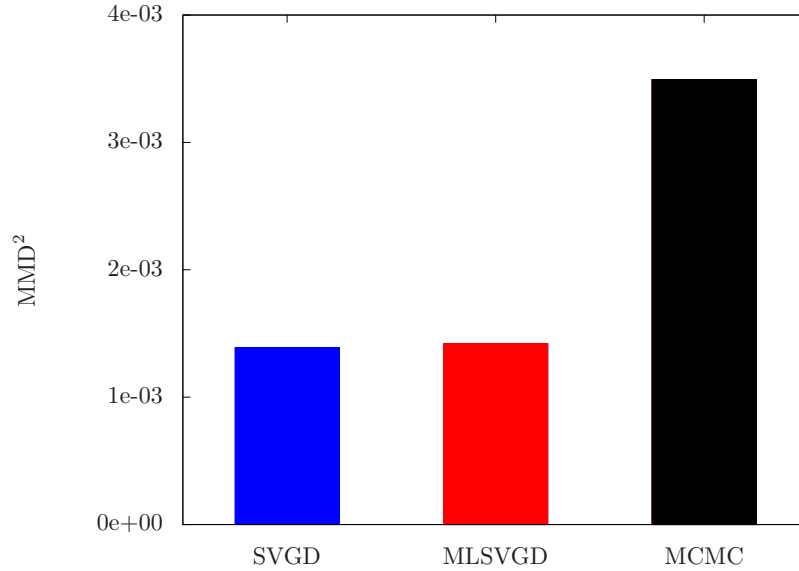


Figure 5: The estimated squared MMD using the estimator (49). The MLSVG approximation has a comparable MMD to the single-level SVGD with the high-fidelity model only. Both have a lower MMD than MCMC suggesting higher quality samples.

where $\{\mathbf{x}_i\}_{i=1}^N \sim \mu$ and $\{\mathbf{y}_j\}_{j=1}^M \sim \nu$. To compute the MMD from the target distribution $\pi^{(L)}$ we use pCN with $\beta = 0.01$ again to draw samples. We use a burn-in period of 20,000 samples and then run 100,000 more iterations taking every 5th sample for 20,000 samples total. These 20,000 samples serve as proxy samples from target posterior $\pi^{(L)}$. Figure 5 shows the estimated MMD for MLSVG, SVGD, and MCMC. We see that MLSVG gives samples with comparable quality to SVGD due to the repulsive interaction between particles, and both SVGD and MLSVG outperform MCMC (pCN) with the same sample size ($N = 1,000$).

5 Conclusion

We provided further analysis of the MLSVG method that extends to regimes where SVGD exhibits a different convergence rate than an exponential one, which greatly increases the scope because SVGD achieves an exponential convergence rate only in limited settings. Based on a Bayesian inverse problem of inferring a discretized basal sliding coefficient field, we also demonstrated that MLSVG scales well to larger settings than the ones considered in prior work [3]. In particular, MLSVG provides particles of comparable quality as SVGD but at greatly reduced computational costs in our numerical example. There are several avenues of future research. One is combining MLSVG with the likelihood-informed projections introduced in [9], which is especially useful in high-dimensional Bayesian inverse problems, where typically data inform only low-dimensional subspaces of the potentially high-dimensional spaces of the quantities of interest.

Acknowledgements

The first and third author acknowledge support from the AFOSR under Award Number FA9550-21-1-0222 (Dr. Fariba Fahroo).

References

- [1] M. S. Alnaes, J. Blechta, J. Hake, A. Johansson, B. Kehlet, A. Logg, C. Richardson, J. Ring, M. E. Rognes, and G. N. Wells. The FEniCS project version 1.5, 2015.

- [2] T. Alsup and B. Peherstorfer. Context-aware surrogate modeling for balancing approximation and sampling costs in multi-fidelity importance sampling and Bayesian inverse problems. *SIAM/ASA Journal on Uncertainty Quantification*, 2022. (accepted).
- [3] T. Alsup, L. Venturi, and B. Peherstorfer. Multilevel Stein variational gradient descent with applications to Bayesian inverse problems. In J. Bruna, J. S. Hesthaven, and L. Zdeborova, editors, *Proceedings of Machine Learning Research*, volume 145 of *2nd Annual Conference on Mathematical and Scientific Machine Learning*, pages 1–25, 2021.
- [4] J. Ba, M. Erdogdu, M. Ghassemi, T. Suzuki, and D. Wu. Towards characterizing the high-dimensional bias of kernel-based particle inference algorithms. In *2nd Symposium on Advances in Approximate Bayesian Inference*, pages 1–17, 2019.
- [5] A. Beskos, A. Jasra, K. Law, R. Tempone, and Y. Zhou. Multilevel sequential Monte Carlo samplers. *Stochastic Processes and their Applications*, 127(5):1417 – 1440, 2017.
- [6] W. Briggs, V. E. Henson, and S. McCormick. *A Multigrid Tutorial, Second Edition*. Society for Industrial and Applied Mathematics, second edition, 2000.
- [7] N. Chada, A. Jasra, and F. Yu. Multilevel ensemble Kalman–Bucy filters. *SIAM/ASA Journal on Uncertainty Quantification*, 10(2):584–618, 2022.
- [8] P. Chen and O. Ghattas. Stein variational reduced basis Bayesian inversion. *SIAM Journal on Scientific Computing*, 43(2):A1163–A1193, 2021.
- [9] P. Chen, K. Wu, J. Chen, T. O. Leary-Roseberry, and O. Ghattas. Projected Stein variational Newton: A fast and scalable Bayesian inference method in high dimensions. In H. Wallach, H. Larochelle, A. Beygelzimer, F. d’ Alché-Buc, E. Fox, and R. Garnett, editors, *Advances in Neural Information Processing Systems*, volume 32, pages 15130–15139. Curran Associates, Inc., 2019.
- [10] S. Chewi, T. L. Gouic, C. Lu, T. Maunu, and P. Rigollet. SVGD as a kernelized Wasserstein gradient flow of the chi-squared divergence. In H. Larochelle, M. Ranzato, R. Hadsell, M. Balcan, and H. Lin, editors, *Advances in Neural Information Processing Systems*, volume 33. Curran Associates, Inc., 2020.
- [11] K. A. Cliffe, M. Giles, R. Scheichl, and A. L. Teckentrup. Multilevel Monte Carlo methods and applications to elliptic PDEs with random coefficients. *Computing and Visualization in Science*, 14(1):3–15, 2011.
- [12] S. L. Cotter, G. O. Roberts, A. M. Stuart, and D. White. MCMC methods for functions: modifying old algorithms to make them faster. *Statist. Sci.*, 28(3):424–446, 2013.
- [13] T. Cui, K. J. Law, and Y. M. Marzouk. Dimension-independent likelihood-informed MCMC. *Journal of Computational Physics*, 304:109–137, 2016.
- [14] G. Detommaso, T. Cui, Y. Marzouk, A. Spantini, and R. Scheichl. A Stein variational Newton method. In S. Bengio, H. Wallach, H. Larochelle, K. Grauman, N. Cesa-Bianchi, and R. Garnett, editors, *Advances in Neural Information Processing Systems*, volume 31, pages 9169–9179. Curran Associates, Inc., 2018.
- [15] T. J. Dodwell, C. Ketelsen, R. Scheichl, and A. L. Teckentrup. A hierarchical multilevel Markov chain Monte Carlo algorithm with applications to uncertainty quantification in subsurface flow. *SIAM/ASA Journal on Uncertainty Quantification*, 3(1):1075–1108, 2015.
- [16] A. Duncan, N. Nuesken, and L. Szpruch. On the geometry of Stein variational gradient descent, 2019.
- [17] M. Giles. Multilevel Monte Carlo path simulation. *Operations Research*, 56(3):607–617, 2008.

- [18] A. Gregory, C. J. Cotter, and S. Reich. Multilevel ensemble transform particle filtering. *SIAM Journal on Scientific Computing*, 38(3):A1317–A1338, 2016.
- [19] A. Gretton, K. Borgwardt, M. Rasch, B. Schölkopf, and A. Smola. A kernel two-sample test. *Journal of Machine Learning Research*, 13:723–773, 2012.
- [20] W. Hackbush. *Multi-Grid Methods and Applications*. Springer, 1985.
- [21] S. Heinrich. Multilevel Monte Carlo methods. In *Proceedings of the Third International Conference on Large-Scale Scientific Computing-Revised Papers, LSSC '01*, pages 58–67. Springer-Verlag, 2001.
- [22] H. Hoel, K. Law, and R. Tempone. Multilevel ensemble Kalman filtering. *SIAM Journal on Numerical Analysis*, 54(3):1813–1839, 2016.
- [23] R. Jordan, D. Kinderlehrer, and F. Otto. The variational formulation of the Fokker–Planck equation. *SIAM Journal on Mathematical Analysis*, 29(1), 1998.
- [24] J. Kaipio and E. Somersalo. Statistical inverse problems: Discretization, model reduction, and inverse crimes. *Journal of Computational and Applied Mathematics*, 198(2):493–504, 2007.
- [25] K.-T. Kim, U. Villa, M. Parno, Y. Marzouk, O. Ghattas, and N. Petra. HIPPylib-MUQ: A Bayesian inference software framework for integration of data with complex predictive models under uncertainty. *arXiv*, 2112.00713, 2021.
- [26] J. Konrad, I.-G. Farcas, B. Peherstorfer, A. Di Siena, F. Jenko, T. Neckel, and H.-J. Bungartz. Data-driven low-fidelity models for multi-fidelity Monte Carlo sampling in plasma micro-turbulence analysis. *Journal of Computational Physics*, 451:110898, 2022.
- [27] A. Korba, A. Salim, M. Arbel, G. Luise, and A. Gretton. A non-asymptotic analysis for Stein variational gradient descent. In *Advances in Neural Information Processing Systems*, volume 33, 2020.
- [28] J. Latz. On the well-posedness of Bayesian inverse problems. *SIAM/ASA Journal on Uncertainty Quantification*, 8(1):451–482, 2020.
- [29] J. Latz, I. Papaioannou, and E. Ullmann. Multilevel sequential² Monte Carlo for Bayesian inverse problems. *Journal of Computational Physics*, 368:154 – 178, 2018.
- [30] Z. Li, Y. Fan, and L. Ying. Multilevel fine-tuning: Closing generalization gaps in approximation of solution maps under a limited budget for training data. *Multiscale Modeling & Simulation*, 19(1), 2021.
- [31] Q. Liu. Stein variational gradient descent as gradient flow. In I. Guyon, U. V. Luxburg, S. Bengio, H. Wallach, R. Fergus, S. Vishwanathan, and R. Garnett, editors, *Advances in Neural Information Processing Systems*, volume 30, pages 3115–3123. Curran Associates, Inc., 2017.
- [32] Q. Liu and D. Wang. Stein variational gradient descent: A general purpose Bayesian inference algorithm. In D. Lee, M. Sugiyama, U. Luxburg, I. Guyon, and R. Garnett, editors, *Advances in Neural Information Processing Systems*, volume 29, pages 2378–2386. Curran Associates, Inc., 2016.
- [33] J. Lu, Y. Lu, and J. Nolen. Scaling limit of the Stein variational gradient descent: The mean field regime. *SIAM Journal on Mathematical Analysis*, 51(2):648–671, 2019.
- [34] M. Lykkegaard, T. Dodwell, C. Fox, G. Mingas, and R. Scheichl. Multilevel delayed acceptance MCMC. *arXiv:2202.03876*, 2022.

- [35] F. Pattyn, L. Perichon, A. Aschwanden, B. Breuer, B. de Smedt, O. Gagliardini, G. H. Gudmundsson, R. C. A. Hindmarsh, A. Hubbard, J. V. Johnson, T. Kleiner, Y. Konovalov, C. Martin, A. J. Payne, D. Pollard, S. Price, M. Ruckamp, F. Saito, O. Soucek, S. Sugiyama, , and T. Zwinger. Benchmark experiments for higher-order and full-Stokes ice sheet models (ISMIP-HOM). *The Cryosphere*, 2:95 – 108, 2008.
- [36] B. Peherstorfer, P. Beran, and K. Willcox. Multifidelity Monte Carlo estimation for large-scale uncertainty propagation. In *2018 AIAA Non-Deterministic Approaches Conference*. AIAA, 2018.
- [37] B. Peherstorfer, M. Gunzburger, and K. Willcox. Convergence analysis of multifidelity Monte Carlo estimation. *Numerische Mathematik*, 139(3):683–707, 2018.
- [38] B. Peherstorfer, B. Kramer, and K. Willcox. Multifidelity preconditioning of the cross-entropy method for rare event simulation and failure probability estimation. *SIAM/ASA Journal on Uncertainty Quantification*, 6(2):737–761, 2018.
- [39] B. Peherstorfer and Y. Marzouk. A transport-based multifidelity preconditioner for Markov chain Monte Carlo. *Advances in Computational Mathematics*, 45:2321–2348, 2019.
- [40] B. Peherstorfer, K. Willcox, and M. Gunzburger. Survey of multifidelity methods in uncertainty propagation, inference, and optimization. *SIAM Review*, 60(3):550–591, 2018.
- [41] N. Petra, J. Martin, G. Stadler, and O. Ghattas. A computational framework for infinite-dimensional Bayesian inverse problems, part II: Stochastic Newton MCMC with application to ice sheet flow inverse problems. *SIAM J. Sci. Comput.*, 36(4):A1525–A1555, 2014.
- [42] A. Stuart. Inverse problems: A Bayesian perspective. *Acta Numerica*, 19:451–559, 2010.
- [43] U. Villa, N. Petra, and O. Ghattas. Documentation to “hIPPYlib: an Extensible Software Framework for Large-scale Deterministic and Bayesian Inverse Problems”, 2016. <http://hippylib.github.io>.
- [44] U. Villa, N. Petra, and O. Ghattas. hIPPYlib: an Extensible Software Framework for Large-scale Deterministic and Bayesian Inverse Problems. *Journal of Open Source Software*, 3(30), 2018.
- [45] U. Villa, N. Petra, and O. Ghattas. HIPPYlib: An Extensible Software Framework for Large-Scale Inverse Problems Governed by PDEs: Part I: Deterministic Inversion and Linearized Bayesian Inference. *ACM Trans. Math. Softw.*, 47(2), Apr. 2021.
- [46] F. Wagner, J. Latz, I. Papaioannou, and E. Ullmann. Multilevel sequential importance sampling for rare event estimation. *SIAM Journal on Scientific Computing*, 42(4):A2062–A2087, 2020.
- [47] D. Wang, Z. Tang, C. Bajaj, and Q. Liu. Stein variational gradient descent with matrix-valued kernels. In *Advances in Neural Information Processing Systems*, volume 32, 2019.